Propagation of CAMS Aerosol Uncertainty to Clear-sky Solar Irradiance Estimates

Anna Moustaka[1], Kyriakoula Papachristopoulou[1], Georgia Charalampous[2,3], and Stelios Kazadzis[1]

[1] Physikalisch Meteorologisches Observatorium, World Radiation Center, Davos, 7260, Switzerland
[2] Department of Resilient Society Eratosthenes Centre of Excellence, Limassol, 3012, Cyprus
[3] Department of Civil Engineering & Geomatics, Cyprus University of Technology, Limassol, 3036, Cyprus

Correspondence to: Anna Moustaka (anna.moustaka@pmodwrc.ch)

Abstract. Atmospheric aerosols strongly influence surface solar radiation (SSR) through scattering and absorption processes, introducing substantial uncertainties into SSR estimates. Atmospheric reanalysis products are increasingly used for solar resource assessment; however, the propagation of aerosol-related uncertainty into SSR calculations remains insufficiently quantified. In this study, we derive aerosol optical depth (AOD) uncertainties for the fourth-generation ECMWF Atmospheric Composition Reanalysis 4 (EAC4) and investigate their propagation into clear-sky estimates of global horizontal irradiance (GHI) and direct normal irradiance (DNI) over the 60°S–60°N domain for the 2003–2024 period. AOD uncertainties are calculated using collocated EAC4 and Aerosol Robotic Network (AERONET) observations, yielding a global mean relative AOD uncertainty of approximately 47%. Radiative kernels are subsequently used to quantify the sensitivity of clear-sky SSR to AOD perturbations, enabling the propagation of AOD uncertainty into GHI and DNI estimates. The results reveal pronounced spatial and seasonal variability, with the largest propagated uncertainties occurring over regions affected by persistent anthropogenic pollution, biomass burning, and desert dust. Relative GHI uncertainties generally remain below 5–6%, whereas relative DNI uncertainties frequently exceed 18% over major aerosol source regions and reach 25–35% seasonally under elevated aerosol loading. Overall, the proposed framework provides a computationally efficient methodology for generating uncertainty-aware solar irradiance products and supports future investigations of aerosol-driven dimming and brightening, as well as long-term solar energy resource assessments under changing atmospheric conditions.

1 Introduction

In 2025, the European Union installed 65.1 GW of new solar photovoltaic (PV) capacity, while cumulative installed capacity is projected to reach approximately 718 GW by 2030 under the medium-growth scenario (SolarPower Europe, 2025). Globally, PV technology is expected to dominate renewable energy expansion through 2030, accounting for nearly 80% of the projected increase in renewable electricity capacity worldwide, while concentrating solar power (CSP) is another promising solar energy technology growing fast in recent years (IEA, 2025). In this context, surface solar radiation (SSR) constitutes a key parameter for solar energy applications, as it directly controls the power generation potential of solar energy systems, thereby strongly

influencing their design, operation, and economic viability (Ahmed et al., 2020; Li et al., 2021; Arnaoutakis et al., 2022). The large-scale deployment of solar energy systems therefore requires accurate characterization of SSR at both regional and global scales, which exhibits substantial spatial and temporal variability (Şen, 2004; Wang et al., 2020; Izam et al., 2022). Among the various factors affecting SSR, atmospheric aerosols play a major role, as they can substantially modify the amount of solar radiation reaching the Earth's surface through scattering and absorption processes associated with their direct radiative effect (Boucher et al., 2013).

The aerosol optical depth (AOD) is commonly used to quantify the attenuation of solar radiation by aerosols, serving as one of the key parameters controlling aerosol radiative effects. Previous studies have shown that discrepancies between modeled and observed solar irradiances are often strongly linked to uncertainties in AOD inputs (Gueymard, 2010; Yang et al., 2022). Aerosol information is commonly derived from both ground-based and satellite observations. Ground-based networks, such as the Aerosol Robotic NETwork (AERONET, Holben et al., 1998) and the Global Atmosphere Watch Precision Filter Radiometer network (GAW-PFR, Kazadzis et al., 2018) generally provide highly accurate aerosol measurements; however, their spatial coverage remains relatively sparse worldwide (Sengupta et al., 2021). In contrast, satellite observations, such as the Moderate Resolution Imaging Spectroradiometer (MODIS; Levy et al., 2010) and the Multi-angle Imaging Spectroradiometer (MISR; Diner et al., 1998), provide near-global spatial coverage and long-term records, making them especially valuable for global aerosol monitoring and solar radiation applications. In parallel, atmospheric reanalyses such as the Modern-Era Retrospective Analysis for Research and Applications, Version 2 (MERRA-2; Buchard et al., 2017; Gelaro et al., 2017), and the Copernicus Atmosphere Monitoring Service (CAMS; Morcrette et al., 2009) combine numerical modeling with the assimilation of diverse observational datasets to provide global aerosol fields with high temporal resolution.

SSR information is currently obtained from several sources, such as ground-based and in-situ observations, reanalysis, models, and satellite retrievals (Gueymard, 1993; Wild et al., 2013; Tang et al., 2019; Jiao et al., 2022; Lu et al., 2023). Ground-based SSR measurements are generally considered the most accurate source of information. High-quality observations are provided by networks such as the Baseline Surface Radiation Network (BSRN; Driemel et al., 2018). These measurements provide high temporal resolution and highly accurate point-scale observations; however, their spatial coverage remains sparse and unevenly distributed worldwide, limiting their ability to resolve the spatial distribution of global horizontal irradiance (GHI) or direct normal irradiance (DNI). In contrast, satellite-derived products and atmospheric reanalyses provide spatially continuous SSR datasets with near-global coverage, making them particularly suitable for climate studies and solar energy applications. Nevertheless, the evaluation of these products against high-quality ground-based observations remains essential for assessing and improving their accuracy and reliability (He et al., 2023; Jiao et al., 2022; Saint-Drenan and Wald, 2025).

Although numerous studies have evaluated the performance of different SSR products against ground-based observations (Zib et al., 2012; Hatzianastassiou et al., 2020; Jiao et al., 2022; He et al., 2023; 2025; Wiltink et al., 2024; Saint-Drenan and Wald, 2025), substantially less attention has been devoted to quantifying how uncertainties in aerosol properties propagate into uncertainties in SSR estimates. This limitation is particularly important for DNI, which is highly sensitive to aerosol attenuation and scattering processes (Hu et al., 2026). In regions characterized by persistent anthropogenic pollution, biomass burning, or

desert dust events, where aerosol effects on clear-sky SSR are particularly pronounced, uncertainties in aerosol characterization, such as the AOD, may therefore propagate into uncertainties in solar radiation products, potentially affecting solar energy assessments (Bartók et al., 2017)

Radiative kernels provide an efficient framework for quantifying the sensitivity of radiative fluxes to perturbations in atmospheric properties and have been widely used in aerosol direct radiative effect (DRE) studies (Soden et al., 2008; Shell et al., 2008; McComiskey et al., 2008; Thorsen et al., 2020, 2021). Such approaches enable the propagation of uncertainties in aerosol properties into uncertainties in radiative quantities while accounting for realistic atmospheric variability. In parallel, several studies have proposed prognostic uncertainty frameworks for AOD retrievals based on collocated satellite and AERONET observations (Sayer et al., 2013), allowing uncertainty estimates to be directly linked to the retrieved aerosol conditions. Nevertheless, most previous studies have primarily focused on aerosol DREs, while a substantial gap still exists in the systematic quantification of how aerosol-related uncertainties propagate into surface solar irradiance components relevant for solar energy applications, particularly GHI and DNI, at global scale and over long-term periods.

To address the limited understanding of how aerosol-related uncertainties propagate into SSR components relevant for solar energy applications, the present study first derives the global AOD uncertainties for the EAC4 using collocated EAC4 and AERONET observations following the expected-error framework of Sayer et al. (2013). These AOD uncertainties were subsequently propagated into clear-sky GHI and DNI estimates over the study domain (60°S–60°N) for the 2003–2024 period. Clear-sky irradiances are obtained using radiative transfer simulations driven by EAC4 aerosol fields together with ancillary atmospheric and surface datasets. The resulting irradiance estimates are evaluated against high-quality ground-based measurements from the BSRN, and the propagated AOD-related irradiance uncertainties are further assessed against the observed EAC4-BSRN irradiance differences. The sensitivity of GHI and DNI to AOD perturbations is quantified through radiative kernels, enabling the propagation of AOD uncertainties into irradiance uncertainty estimates. The analysis investigates the spatial and seasonal variability of the resulting GHI and DNI uncertainties and their dependence on aerosol loading at the global scale. In addition, station-level analyses are performed for the highest-ranked AERONET stations in terms of long-term aerosol loading to investigate the temporal variability and magnitude of aerosol-related irradiance uncertainties under extreme aerosol environments.

2 Data and Methodology

2.1 Reanalysis aerosol data

The Copernicus Atmosphere Monitoring Service (CAMS; https://atmosphere.copernicus.eu; last access: 07 July 2026) is a major component of the European Union's Copernicus Earth observation programme, providing global products of atmospheric composition, including aerosols and reactive trace gases. The ECMWF Atmospheric Composition Reanalysis 4 (EAC4) was first released in 2017, with the historical record for 2003–2019 completed in 2020 and subsequently extended to the present

(Langerock et al., 2024). At the time of this study, the dataset covered the period from 2003 to August 2025, while the present analysis covers the period 2003–2024.

EAC4 is produced using the European Centre for Medium-Range Weather Forecasts (ECMWF) Integrated Forecasting System (IFS), coupled with the Carbon Bond 2005 (CB05) atmospheric chemistry mechanism (Huijnen et al., 2010; Flemming et al., 2015). The aerosol component represents the major atmospheric aerosol species, including desert dust, sea salt, sulfate, organic matter, and black carbon, together with their relevant physical and chemical processes. Aerosol emissions are derived from a combination of online parameterizations for natural sources and external inventories for anthropogenic and biomass-burning emissions, including GFAS and MACCity (Morcrette et al., 2009; Kaiser et al., 2012; Granier et al., 2011).

In this study, the EAC4 total aerosol optical depth (AOD) at 550 nm data were retrieved from the Copernicus Atmosphere Data Store (https://ads.atmosphere.copernicus.eu/; last access: 07 July 2026) at a spatial resolution of 0.75° × 0.75° and a temporal resolution of 3 hours.

2.2 Ground-based aerosol observations

Ground-based aerosol observations were obtained from the Aerosol Robotic Network (AERONET; Holben et al., 1998, 2001), which operates a worldwide network of sun photometers providing long-term measurements of column-integrated aerosol properties. Version 3 (V3) Level 2.0 AERONET data were used in the present analysis. These data undergo automated cloud screening and quality assurance control and have estimated aerosol optical depth (AOD) uncertainties of approximately ±0.01 at visible wavelengths and ±0.02 in the ultraviolet (Giles et al., 2019; Sinyuk et al., 2020). AERONET measurements are available at multiple wavelengths between approximately 340 and 1640 nm and at a temporal sampling of typically 5–15 min. For the present study, AERONET serves as the observational reference for characterizing the uncertainty of EAC4 AOD. The analysis uses the same set of stations and data-selection criteria previously employed by Moustaka et al. (2026) for the 2003–2024 period. Briefly, these criteria were designed to ensure sufficient temporal coverage and long-term representativeness of the observations. The complete filtering procedure and associated data-availability requirements are provided by both Zhang et al. (2025) and Moustaka et al. (2026) and are therefore not repeated here. Mauna Loa and Mexico City were additionally excluded following Inness et al. (2019), owing to known difficulties in the representation of volcanic sulfate in global aerosol modelling (Huijnen et al., 2010; Inness et al., 2019). The resulting observational dataset comprises 178 AERONET stations distributed across a broad range of aerosol environments.

AERONET observations are not directly assimilated into EAC4, which assimilates satellite-derived AOD observations (Langerock et al., 2024). Therefore, AERONET provides an independent ground-based reference for the evaluation of EAC4 AOD. However, because EAC4 AOD is analysed at 550 nm, whereas AERONET does not provide a direct measurement at this wavelength, the AERONET observations were spectrally interpolated to 550 nm using the Ångström power-law relationship (Ångström, 1929):

$$AOD_{\lambda} = AOD_{\lambda 0} \cdot \left(\frac{\lambda_0}{\lambda}\right)^{\acute{a}}, \quad (1)$$

where $\lambda = 550$ nm, $\lambda_0 = 440$ nm, and $\dot{a}$ is the Ångström exponent derived from AOD measurements in the 440–675 nm spectral range (Eck et al., 1999; Giles et al., 2019).

2.3 Radiative transfer simulations

Radiative fluxes were derived at 1-hourly temporal resolution using a lookup table (LUT) approach based on radiative transfer model (RTM) simulations performed with the UVSPEC model of the libRadtran radiative transfer package (Emde et al., 2016). The LUT used in this study follows the framework described in Papachristopoulou et al. (2024). Rather than performing computationally expensive RTM simulations for every grid cell and time step, radiative fluxes were obtained by interpolation within a set of pre-computed RTM simulations stored in the LUT. The use of LUTs as a computationally efficient alternative to direct RTM calculations is well established in solar radiation retrievals (Mueller et al., 2009; Qu et al., 2017). The interpolation approach has been shown to provide results that are nearly identical to direct RTM calculations while substantially reducing computational cost (Papachristopoulou et al., 2022; 2024).

The LUT consists of pre-calculated radiative fluxes, including global horizontal irradiance (GHI) and direct normal irradiance (DNI), generated for a range of atmospheric and surface conditions. Specifically, the LUT is seven-dimensional and constructed as a function of aerosol optical depth (AOD), solar zenith angle (SZA), single scattering albedo (SSA), Ångström exponent (AE), total column ozone (TCO), total column water vapour (TCWV), and surface albedo (ALB). These parameters describe the state of the atmosphere, as well as the radiative properties of the surface, and were used as input to the RTM-based LUT framework.

For the aerosol information, 3-hourly AOD fields were obtained from the EAC4 global atmospheric reanalysis dataset (Inness et al., 2019). The EAC4 dataset combines model simulations with assimilated satellite aerosol observations and provides spatially and temporally continuous atmospheric fields suitable for long-term radiative applications. Monthly climatological fields of SSA and AE were obtained from the AeroCom dataset (Kinne, 2019), which provides globally consistent aerosol optical properties climatology.

Trace gas parameters required as input to the LUT were derived from monthly 3-hourly mean EAC4 fields. Specifically, TCWV and TCO were represented by separate monthly mean fields for each 3-hourly UTC time step (00:00, 03:00, 06:00, …, 21:00 UTC) (Inness et al., 2019). This approach retains the mean seasonal and diurnal variability of TCWV and TCO while reducing the computational requirements of the global 2003–2024 calculations. Surface albedo information was derived from the HAMSTER dataset (Roccetti et al., 2024). The HAMSTER surface albedo at 550 nm was used as input to the LUT and was assumed to be spectrally constant across the wavelength range of the radiative transfer calculations. Due to the presence of seasonally dependent missing values in the HAMSTER albedo dataset at high latitudes, the present analysis was restricted to the latitude band between 60° S and 60° N. This restriction ensures consistent spatial coverage across seasons and avoids introducing artefacts related to incomplete surface albedo information. Finally, SZA values were calculated from solar geometry for each grid cell and updated hourly, whereas the remaining atmospheric and surface input parameters were assumed constant within each 3-hourly interval. Radiative fluxes were calculated at hourly temporal resolution. Since EAC4 AOD is

available every 3 hours, the nearest AOD field was assigned to each hourly time step (i.e. each AOD value was assumed constant within ±1.5 h of its nominal analysis time), while SZA was recalculated for every hour to account for the changing solar geometry.

To ensure spatial consistency among the various input datasets, all parameters (SSA, AE, TCO, TCWV, and ALB) were regridded to the native spatial resolution of the EAC4 AOD dataset (0.75° × 0.75°) prior to their use in the LUT framework. Afterwards, the radiative fluxes were estimated through interpolation within the LUT for each grid cell and time step. A schematic overview of the overall methodology and data flow is presented in Fig. 1, while a summary of the datasets and temporal resolutions used in this study is provided in Table 1. Following Papachristopoulou et al. (2024), the LUT-derived radiative fluxes correspond initially to sea-level conditions and mean Earth–Sun distance. Therefore, an additional post-processing correction was applied to account for surface elevation and the actual Earth–Sun distance corresponding to each day of year (DOY). The elevation correction follows the methodology of Fountoulakis et al. (2021), who estimated an average increase of approximately 2 % per kilometre in clear-sky GHI under different atmospheric and surface conditions. This correction was subsequently applied to the LUT-derived radiative fluxes in order to account for altitude-dependent effects on surface solar irradiance.

Radiative quantities were obtained through interpolation within the 7D LUT. Specifically, for each grid cell (i, j) and time (t), the radiative flux was derived by interpolating within the pre-computed LUT using the corresponding values of AOD, SZA, SSA, AE, TCO, TCWV, and ALB (Fig. 1). The LUT-derived radiative fluxes were subsequently used to compute radiative kernels (as described in Sect. 2.5), which quantify the sensitivity of surface solar radiation to AOD perturbations. These kernels form the basis for the propagation of AOD uncertainty into uncertainties in surface radiative fluxes.

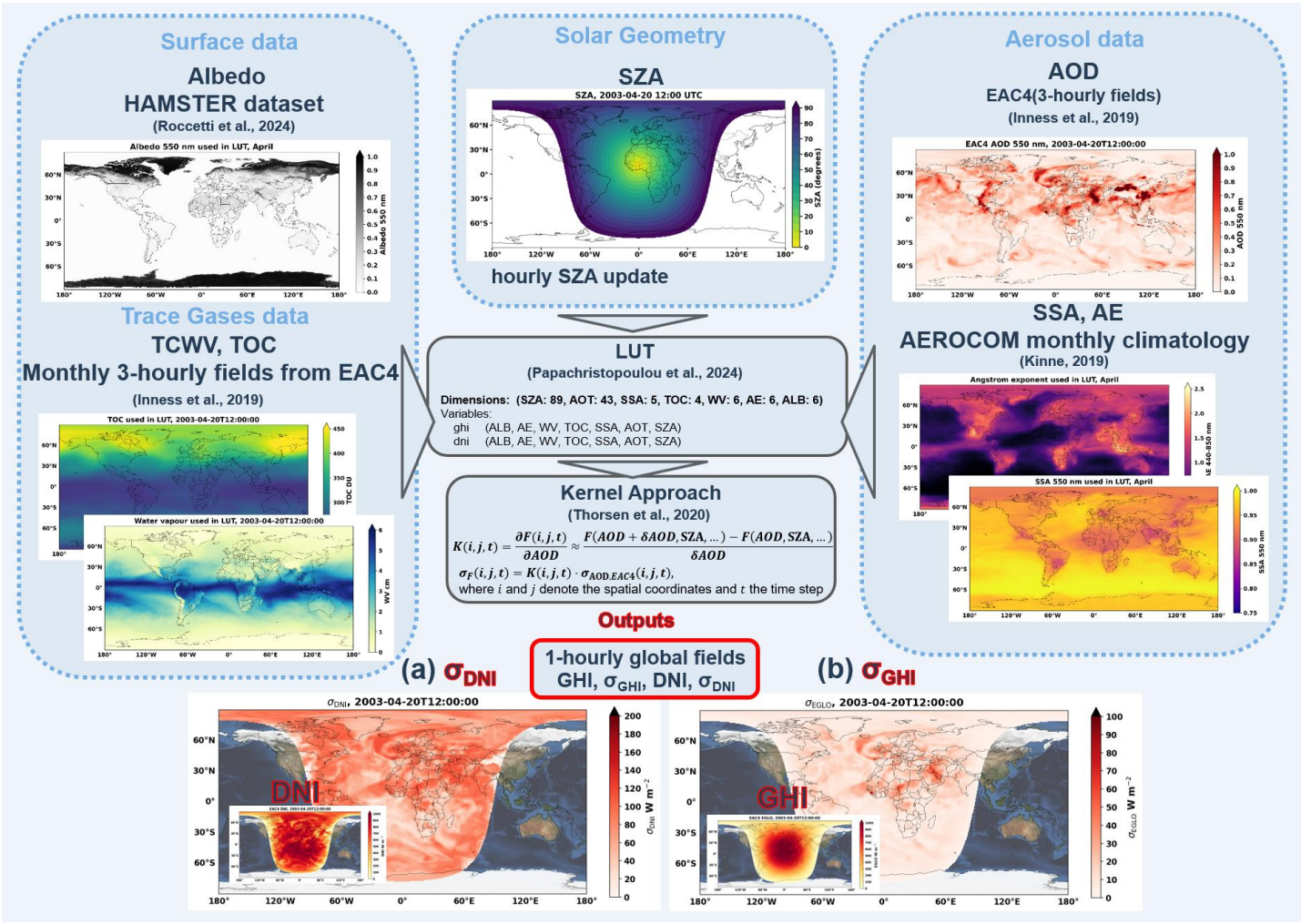

Figure 1: Schematic overview of the LUT-based methodology used to estimate hourly global radiative fluxes and their associated uncertainties. The LUT simulations are driven by aerosol, atmospheric, surface, and solar geometry inputs, including AOD, SSA, AE, TCWV, TCO, ALB, and SZA. The LUT outputs include GHI, DNI, and their associated uncertainty estimates. Map source: NASA Earth Observatory.

Table 1: Overview of the input parameters used in the radiative transfer lookup table (LUT), including their temporal resolution and corresponding datasets. The table summarizes the atmospheric and surface variables employed for the estimation of surface solar irradiances and the propagation of AOD-related uncertainties.

Input Parameter	Temporal resolution	Dataset
AOD	3-hourly reanalysis fields	EAC4 (https://ads.atmosphere.copernicus.eu/datasets/cams-global-reanalysis-eac4, last access: 04 June 2026; Inness et al., 2019)
SZA	Hourly	Computed from solar geometry
SSA	Monthly climatology	AEROCOM (Kinne, 2019)
AE	Monthly climatology	AEROCOM (Kinne, 2019)

TCWP	Monthly 3-hourly climatology	EAC4 monthly averaged fields (https://ads.atmosphere.copernicus.eu/datasets/cams-global-reanalysis-eac4-monthly, last access: 04 June 2026; Inness et al., 2019)
TCO	Monthly 3-hourly climatology	EAC4 monthly averaged fields (https://ads.atmosphere.copernicus.eu/datasets/cams-global-reanalysis-eac4-monthly, last access: 04 June 2026; Inness et al., 2019)
ALB	Monthly climatology	HAMSTER dataset (Roccetti et al., 2024)

2.4 Estimation of AOD uncertainty

The uncertainties of the EAC4 AOD product were estimated using an expected-error (EE) approach following Sayer et al. (2013). In this framework, the EE is derived from the statistical distribution of differences between the reanalysis AOD (i.e., EAC4) and ground-based AERONET observations and is expressed as a function of the EAC4 AOD. It should be noted that the EAC4–AERONET differences do not exclusively represent errors in the EAC4 AOD but may also include contributions from spatial and temporal representativeness differences, collocation uncertainties, and limitations in the model representation of aerosol properties and their vertical distribution. Consequently, the derived EE should be interpreted as an empirical estimate of EAC4 AOD uncertainty relative to AERONET observations, rather than a direct measure of the intrinsic uncertainty of the reanalysis. Prior to the uncertainty analysis, the performance of EAC4 against 178 AERONET stations worldwide was evaluated by Moustaka et al. (2026), demonstrating generally very good agreement with the observations (R = 0.84, RMSE = 0.12, MAE = 0.07, RMB = 1.0, and IOA = 0.9, based on 1,657,564 collocated data pairs; see Moustaka et al. (2026) for further details on the collocation procedure).

Collocated AOD differences between EAC4 and AERONET were calculated and grouped into bins according to the corresponding EAC4 AOD values, with each bin containing 500 collocated pairs. Within each bin, the distribution of absolute differences $|\Delta\mathrm{AOD}| = |\mathrm{AOD}_{\mathrm{EAC4}} - \mathrm{AOD}_{\mathrm{AERONET}}|$, was analysed. The 68th percentile of this distribution was used as a proxy for the EE, corresponding to one standard deviation under the assumption of an approximately Gaussian error distribution.

A linear model was then fitted to describe the dependence of EE on EAC4AOD:

$$EE = a + b \cdot \mathrm{AOD}_{\mathrm{EAC4}}, \quad (2)$$

where a and b are regression coefficients, and AOD_{EAC4} denotes the median EAC4 AOD within each equal-population bin. To assess the sensitivity of the derived EE relationship to the bin size and the selected fitting function, additional tests were performed using 250, 500, 1,000, and 2,000 observations per bin, as well as a second-order polynomial fit. The fitted linear coefficients showed only minor variations across the different bin sizes, resulting in differences in the estimated AOD uncertainty generally below 1% over the examined AOD range. The quadratic fit slightly reduced the RMSE of the binned EE estimates from 0.00732 to 0.00714 compared with the linear fit, while the resulting differences in AOD uncertainty remained within approximately −3.4% to +1.0% for AOD values between 0.05 and 2.0. These results indicate that the derived uncertainty estimates are relatively insensitive to the selected bin size and fitting function, supporting the use of the original linear parameterization.

The EE–AOD relationship resulting from this procedure is presented in Fig. 2. Additionally, Fig. S1 presents the histograms of the normalized EAC4 AOD error, $\mathrm{AOD_{EAC4}} - \mathrm{AOD_{AERONET}}/\mathrm{EE}$, which are compared against an idealized Gaussian distribution with zero mean and unit variance, namely $\mathcal{N}(0,1)$. The normalized-error distribution exhibits a slight negative bias and broader tails than the theoretical Gaussian distribution, although framing the EAC4–AERONET differences in terms of EE results in a substantially closer correspondence with the idealized Gaussian behaviour. This further demonstrates the general validity of Eq. (2) for the present dataset, while also indicating that the simple linear parameterization does not fully capture the largest-error cases as discussed also in Sayer et al. (2013). Such deviations may be particularly relevant under extreme aerosol conditions that are not fully represented by the global AOD-dependent parameterization.

To obtain the uncertainty of EAC4 AOD ($\sigma_{\mathrm{AOD,EAC4}}$), the contribution of AERONET measurement uncertainty ($\sigma_{\mathrm{AOD,\,AER}}$) was removed in quadrature. A constant AERONET AOD uncertainty ($\sigma_{\mathrm{AOD,AER}}$) of 0.01 was adopted as a first-order approximation based on the reported accuracy of quality-assured AERONET measurements at visible wavelengths (Giles et al., 2019; Sinyuk et al., 2020). This approach assumes that the AERONET measurement uncertainty can be represented as an independent random contribution, expressed in terms of one standard deviation, to the EAC4–AERONET differences. Although the actual AERONET uncertainty may vary among wavelengths, stations, and aerosol conditions, the use of a constant value provides a simplified treatment across the global dataset.

The resulting EAC4 AOD uncertainty ($\sigma_{\mathrm{AOD,EAC4}}$) is given by:

$$\sigma_{\mathrm{AOD,\,EAC4}} = \sqrt{EE^2 - \sigma^2_{\mathrm{AOD,\,AER}}}\,. \tag{3}$$

Substituting the corresponding EE parameterization yields:

$$\sigma_{\mathrm{AOD,\,EAC4}} = \sqrt{(a + b \cdot \mathrm{AOD}_{EAC4})^2 - (0.01)^2}. \tag{4}$$

As presented in Fig. 2, the fitted coefficients were estimated as $a = 0.021$ and $b = 0.318$ based on 1,666,328 collocated EAC4–AERONET observations during the 2003–2024 period. For these fitted coefficients and non-negative AOD values, $a + b \cdot \mathrm{AOD}_{EAC4}$ is always greater than 0.01, ensuring that the quantity under the square root in Eq. (4) remains non-negative. This formulation provides a statistically derived, AOD-dependent estimate of uncertainty for EAC4, allowing the estimated uncertainty to increase with aerosol loading. The parameterization represents the statistical distribution of EAC4–AERONET differences over the 2003–2024 period rather than a dynamically estimated uncertainty for individual atmospheric conditions. Although the resulting uncertainty varies in space and time according to the corresponding EAC4 AOD, the fitted coefficients are applied uniformly across the study domain and period and therefore do not explicitly account for possible dependencies of the EAC4 error on geographical region, season, aerosol type, or other atmospheric conditions. Consequently, the estimated uncertainty should be interpreted as an expected statistical uncertainty conditional on EAC4 AOD.

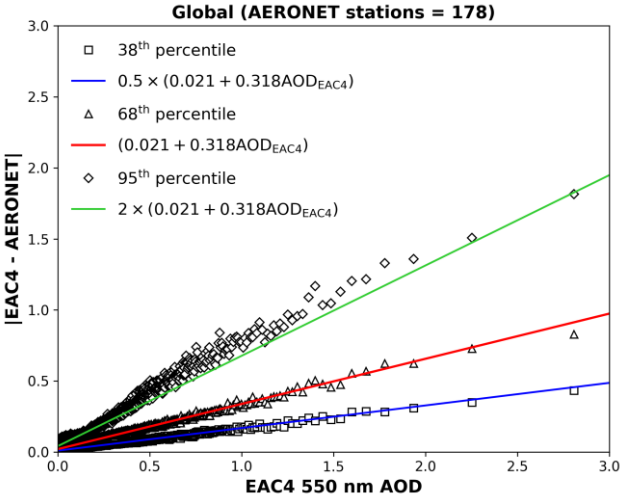

Figure 2: The 38th (squares), 68th (triangles), and 95th (diamonds) percentiles of the absolute differences between EAC4 AOD 550 nm and reference AERONET observations, are shown as a function of the EAC4. The red line represents the least-squares linear fit to the 68th percentile values, while the blue and green lines correspond to one-half and twice the fitted relationship, respectively.

2.5 Propagation of AOD Uncertainty to Surface Radiative Fluxes

The impact of AOD uncertainty on calculating clear-sky irradiances was quantified using a first-order uncertainty propagation approach based on radiative kernels, Thorsen et al. (2020). The analysis focuses on the two main components of SSR, namely GHI and DNI under clear-sky conditions.

The methodology follows a linear approximation, assuming that small perturbations in AOD lead to proportional changes in the radiative flux. Under this assumption, the uncertainty in a radiative flux F due to uncertainty in AOD can be expressed as:

$$\sigma_F = \left| \frac{\partial F}{\partial \mathrm{AOD}} \right| \cdot \sigma_{\mathrm{AOD,EAC4}}, \tag{5}$$

where $\sigma_{\mathrm{AOD,EAC4}}$ is the AOD uncertainty derived as described in Sect. 3.1, and $\frac{\partial F}{\partial \mathrm{AOD}}$ represents the sensitivity of the radiative flux to AOD, hereafter referred to as the radiative kernel.

Radiative kernels were computed using finite differences based on pre-calculated radiative transfer simulations, following the methodology of Thorsen et al. (2020). Specifically, the kernel is approximated as:

$$K(i,j,t) = \frac{\partial F(i,j,t)}{\partial \mathrm{AOD}} \approx \frac{F(\mathrm{AOD} + \delta\mathrm{AOD}, \mathrm{SZA}, \mathrm{AE}, \mathrm{SSA}, \mathrm{TCWV}, \mathrm{TCO}, \mathrm{ALB}) - F(\mathrm{AOD}, \mathrm{SZA}, \mathrm{AE}, \mathrm{SSA}, \mathrm{TCWV}, \mathrm{TCO}, \mathrm{ALB})}{\delta\mathrm{AOD}}, \tag{6}$$

where F denotes the radiative flux (i.e., GHI or DNI), SZA is the solar zenith angle, AE is the Ångström exponent, SSA is the single scattering albedo, $TCWV$ is the total column water vapor, TCO is the total column ozone, ALB is the albedo, and δAOD is a small perturbation in AOD. Specifically, the δAOD perturbation is chosen as a 1% increase to the AOD value following other studies in the literature (e.g., Thorsen et al., 2020; Witthuhn et al., 2021)

For each grid cell and time, the propagated uncertainty in the radiative flux was estimated at the native resolution of the analysis. For each observation, the corresponding kernel value was derived by interpolating within the LUT according to the different input parameters.

The resulting kernel was then combined with the respective $\sigma_{\mathrm{AOD,EAC4}}$ to estimate the propagated uncertainty in the radiative flux, following:

$$\sigma_F(i,j,t) = |K(i,j,t)| \cdot \sigma_{\mathrm{AOD,EAC4}}(i,j,t), \tag{7}$$

where i and j denote the spatial coordinates and t the time step.

2.6 BSRN

The EAC4-derived clear-sky irradiance estimates were evaluated against SSR observations obtained from the Baseline Surface Radiation Network (BSRN), a global network of reference stations providing high-quality, quality-controlled measurements of solar and terrestrial radiation for climate monitoring, model evaluation, and satellite product validation (Ohmura et al., 1998; Driemel et al., 2018). Minute-resolution measurements of SSR components from all available BSRN stations were retrieved through the BSRN FTP archive and processed using the pvlib Python library (Holmgren et al., 2018; Jensen et al., 2023). For each station, all available observations between 2003 and 2024 were extracted and combined into continuous station-specific time series, resulting in a harmonized multi-site dataset spanning a wide range of climatic and geographical conditions. Consistent with the geographical domain adopted throughout this study (Sect. 2.3), only stations located within the latitude band between 60° S and 60° N were considered, reflecting the latitudinal restriction imposed by the availability of the surface albedo dataset used in the irradiance calculations.

To identify clear-sky conditions suitable for the validation of the EAC4-derived irradiance products, the automated clear-sky detection algorithm of Long and Ackerman (2000) was applied. The method identifies clear-sky periods through four complementary tests based on (i) the normalized GHI magnitude, (ii) the maximum allowable diffuse irradiance (DHI) as a function of SZA, (iii) the temporal variability of GHI, and (iv) the temporal variability of the normalized DHI-to-GHI irradiance ratio. Only measurements satisfying all four criteria were retained as clear-sky observations.

The original Long and Ackerman (2000) thresholds were developed empirically for the datasets considered in that study and were described by the authors as subjective quantities that allow a certain degree of flexibility depending on the characteristics of the measurements. Accordingly, the same four filtering tests were adopted here, while several of the empirical threshold values were moderately relaxed following visual inspection of the global BSRN dataset to improve the detection of stable clear-sky periods across different climatic regions without altering the underlying methodology. The modified thresholds consisted of a normalized GHI exponent of 1.10, normalized GHI limits of 1600, 900 and 750 W m^{-2}, a maximum DHI of 250 W m^{-2}, a temporal variability offset of 6 W m^{-2}, and a normalized diffuse-ratio variability threshold of 0.004 using an 11-minute moving window.

Following the clear-sky detection, only measurements acquired within ±5 minutes of each hourly timestamp (e.g., 13:00, 14:00 UTC) were considered. Hourly clear-sky irradiance values were computed by averaging the available 1-minute observations

within each 11-minute window, provided that at least 8 valid clear-sky measurements were present. This requirement ensured sufficient temporal sampling while avoiding time intervals represented by only a few isolated measurements. After applying these quality-control criteria, a total of 64 BSRN stations with 553,184 averaged clear-sky hourly collocations were retained for the analysis. Their spatial distribution and hourly data availability are presented in Fig. S2.

3 Results

3.1 Global Climatology of Mean AOD and Estimated AOD Uncertainty

Figure 3 presents the spatial distribution of the annual mean AOD at 550 nm from the EAC4 for the 2003–2024 period, together with the corresponding estimated uncertainty. Elevated AOD values are primarily observed over regions affected by strong anthropogenic and industrial emissions, particularly eastern China and India, as well as over areas strongly influenced by biomass-burning activity, including Central Africa, the Amazon Basin, and parts of Indonesia. High aerosol loadings are also evident over the major global dust source regions, such as North Africa, the Middle East, Central Asia, and eastern Asia, which together contribute nearly 88 % of global dust emissions (Kok et al., 2023).

It should be noted that locally enhanced AOD values over regions such as Mauna Loa and Mexico City should be interpreted with caution, as they are not fully representative of background aerosol conditions. As discussed in Sect. 2.2, these features are mainly associated with known model biases related to the injection of volcanic sulfur dioxide (SO_2) at unrealistically low altitudes. Under these conditions, SO_2 is more efficiently converted into sulfate aerosols through the sulfur oxidation pathways implemented in the CAMS IFS (CB05) chemical scheme, resulting in an overestimation of sulfate AOD over volcanic regions (Huijnen et al., 2010; Inness et al., 2019).

The global mean AOD is 0.16, with the highest values exceeding 1.3 over intense aerosol source regions. The estimated uncertainty field generally follows the spatial distribution of AOD, with larger uncertainty values occurring over regions characterized by persistently high aerosol loading. The mean estimated AOD uncertainty is 0.07, while the highest values exceed 0.4 locally (e.g., eastern China). The corresponding mean relative AOD uncertainty is approximately 47%. Owing to the EE parameterization used to estimate AOD uncertainty (see Eq. (4)), the relative AOD uncertainty can exceed 100% over very clean regions where the nearly constant absolute uncertainty is divided by very small AOD values.

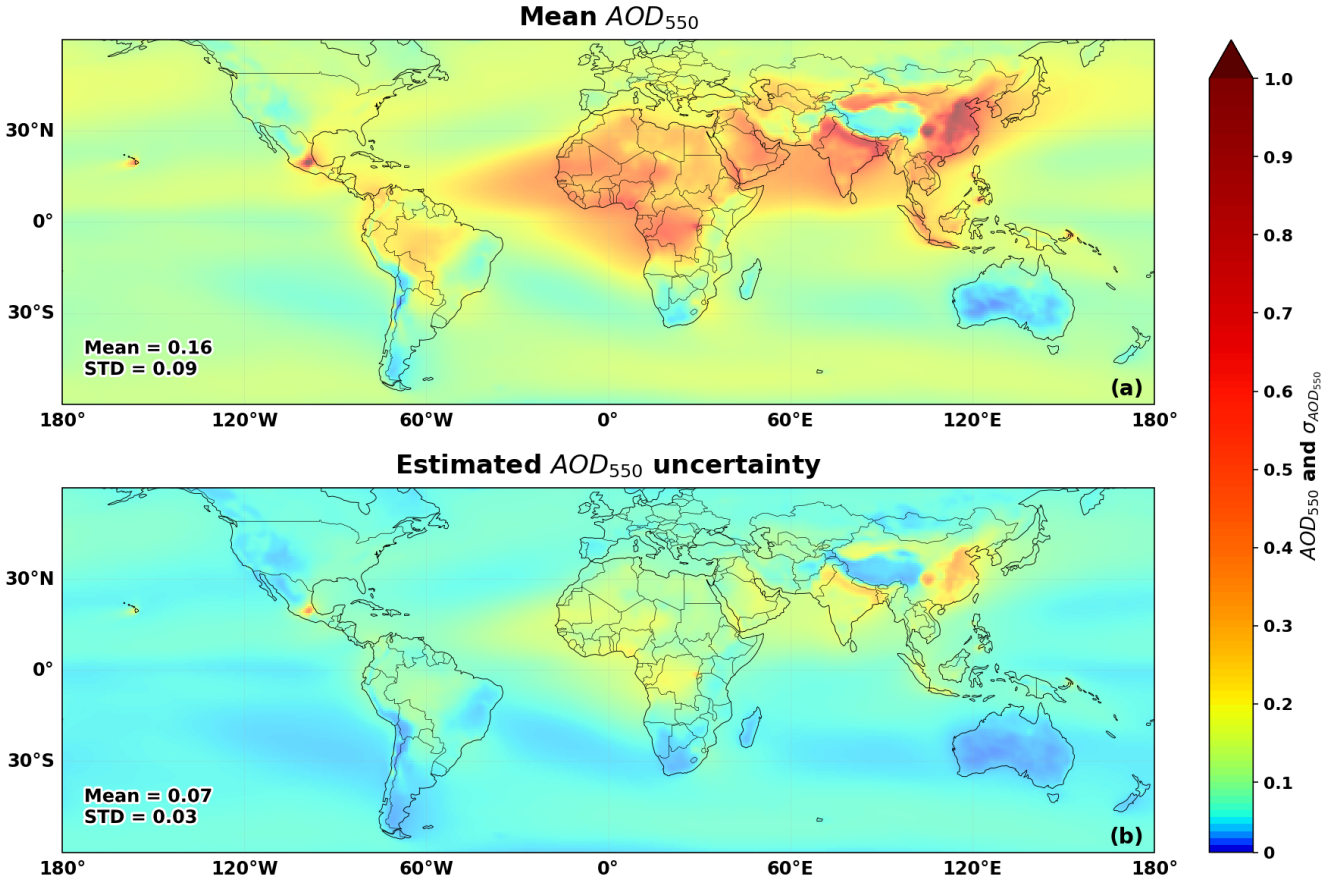

320 **Figure 3: Geographical distribution of (a) the mean-annual AOD at 550 nm based on EAC4 over the 2003–2024 period, and (b) the corresponding estimated AOD uncertainty.**

3.2 Global Distribution of clear-sky GHI, DNI and Associated Uncertainties

Figure 4 presents the global spatial distribution of the mean annual clear-sky GHI and DNI, expressed in W m^{-2}, together with their corresponding relative uncertainties derived from EAC4 AOD uncertainties for the 2003–2024 period. Panels (a) and (c) 325 show the mean annual GHI and DNI, respectively, while panels (b) and (d) present the corresponding relative uncertainties. The corresponding seasonal distributions of GHI, DNI, and their associated relative uncertainties are provided in Figures S3–S6 of the Supplement. It should be emphasized that these uncertainty estimates quantify only the propagation of AOD uncertainty under clear-sky conditions. Uncertainties associated with clouds and other atmospheric or surface input parameters are outside the scope of the present analysis and are therefore not included.

330 As shown in Fig. 4a, the highest GHI values are observed within the tropical and subtropical latitude band between approximately 30° S and 30° N, where incoming solar radiation is maximized due to favourable solar geometry throughout the year. Lower GHI values are evident toward higher latitudes as a result of reduced solar elevation angles and shorter daylight

duration. Compared to GHI, the spatial distribution of DNI (Fig. 4c) exhibits stronger regional variability, reflecting the enhanced sensitivity of the direct solar component to aerosol loading and atmospheric attenuation processes. High DNI values are generally associated with high-altitude and relatively pristine regions characterized by persistent clear-sky conditions, such as the Rocky Mountains in western North America and other elevated terrain with low aerosol loading (Xu et al., 2016). In contrast, regions affected by elevated aerosol concentrations, including areas influenced by anthropogenic pollution (e.g., eastern China and South Asia) and mineral dust (e.g., parts of North Africa and the Middle East), exhibit noticeable reductions in DNI (Papachristopoulou et al., 2022).

Based on Fig. 4b, the relative uncertainties associated with GHI remain comparatively low on a global scale, generally below 5–6 %. Elevated uncertainties are mainly confined to regions characterized by enhanced aerosol loading, including the Sahara, the Arabian Peninsula, the Indo-Gangetic Plain, and parts of East Asia. This relatively weak sensitivity reflects the fact that GHI includes both direct and diffuse irradiance components, making the total downward shortwave flux less sensitive to uncertainties in aerosol attenuation alone.

In contrast, the relative uncertainties associated with DNI are substantially larger and exhibit a much stronger spatial dependence on aerosol conditions (see Fig. 4d). Relative uncertainties exceeding 18 % occur primarily over regions affected by elevated aerosol loading, including areas influenced by mineral dust in North Africa and the Middle East, as well as regions with persistent anthropogenic pollution in South and East Asia. Localized maxima are also evident in areas affected by recurrent biomass-burning activity. These enhanced uncertainty levels reflect the strong sensitivity of the direct solar beam to aerosol extinction processes, which directly modulate the amount of unscattered solar radiation reaching the surface.

The seasonal climatology presented in Figures S3–S6 indicates that the annual patterns are strongly modulated by both solar geometry and seasonal aerosol variability. Seasonal mean GHI follows the expected migration of maximum solar irradiation between hemispheres, with enhanced values over the Southern Hemisphere during DJF and over the Northern Hemisphere during JJA (Fig. S3). In contrast, the spatial distribution of DNI and its associated uncertainty is more strongly influenced by regional aerosol conditions. Elevated relative uncertainties persist throughout the year over major dust sources and pollution hotspots, including North Africa, the Arabian Peninsula, the Indo-Gangetic Plain and eastern China, while the largest seasonal enhancements occur during periods of increased aerosol loading (Fig. S6). Although the seasonal mean relative GHI uncertainty remains comparatively stable (~2% globally) (Fig. S4), the corresponding DNI uncertainty exhibits a stronger seasonal signal, with regional maxima exceeding 25–35% in regions with higher aerosol loads (Fig. S6). These seasonal patterns further support the dominant role of aerosol uncertainty in controlling the reliability of direct solar irradiance estimates.

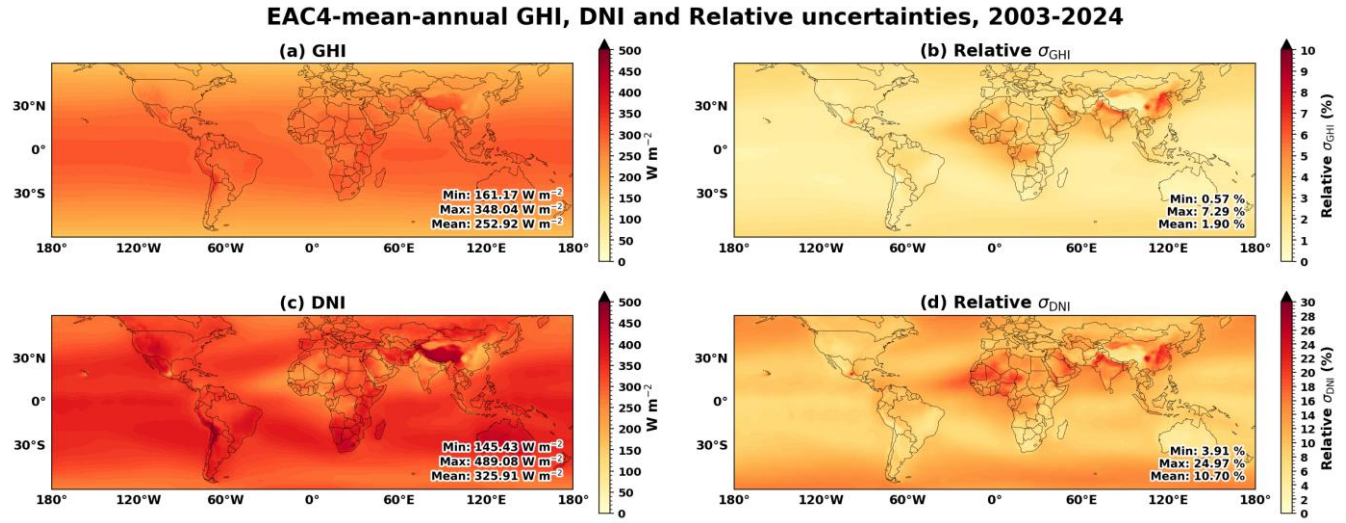

Figure 4: Spatial distribution of mean-annual global horizontal irradiance (GHI), direct normal irradiance (DNI), and their corresponding relative uncertainties for the period 2003–2024. Panels (a) and (c) show the annual mean GHI and DNI, respectively, expressed in W m^{-2}, while panels (b) and (d) present the corresponding relative uncertainties (%).

3.3 High-AOD Stations and Propagation of Aerosol Uncertainty into Surface Solar Irradiance

Additionally, the analysis focused on the 10 AERONET stations characterized by the highest mean AOD values over the 2003–2024 period. The station ranking was based on long-term mean AOD derived from AERONET observations, enabling the identification of regions where aerosol effects on solar radiation are expected to be particularly pronounced. The geographical characteristics and long-term mean AOD values of these stations are summarized in Table S1. The ranking of the top 10 high-AOD AERONET stations, together with their global spatial distribution over the background EAC4 AOD climatology, is provided in Fig. S7. These stations are primarily located in regions strongly influenced by anthropogenic pollution, biomass-burning, and desert dust events, including South Asia, East Asia, and North/West Africa. Figure 5 presents the 10 highest-ranked stations, including Gandhi College, XiangHe, Beijing, Lahore, Ilorin, and Kanpur, which represent some of the most persistently aerosol-loaded environments included in the long-term analysis. The grey line corresponds to EAC4 AOD at 550 nm, while the orange and red lines represent GHI and DNI. The shaded regions indicate the propagated uncertainties associated with each irradiance component resulting from the adopted AOD uncertainty formulation as described in Sect. 2.

Overall, the selected stations exhibit persistently elevated aerosol conditions throughout the year, with long-term mean AOD values ranging from 0.40 to 0.78. The corresponding mean AOD uncertainties range between 0.15 and 0.27, yielding relatively consistent relative AOD uncertainties of approximately 34.5–37.0% across all stations. These enhanced aerosol loadings are consistent with the strong seasonal variability observed over major dust, biomass-burning, and anthropogenic emission regions discussed previously. In particular, stations influenced by dust outbreaks typically exhibit maximum AOD values during boreal spring and summer, reflecting the enhanced dust mobilization and transport occurring between March and August (Stuut et al., 2014; Gkikas et al., 2015) (e.g., Dakar and Banizoumbou). Similarly, stations located in South and East Asia frequently

display pronounced seasonal aerosol peaks associated with severe anthropogenic pollution episodes and biomass-burning activity (Gui et al., 2021), although recent years are characterized by declining aerosol signals over eastern China due to emission control measures (e.g., Beijing and XiangHe), while aerosol loadings over South Asia remain persistently elevated or continue to increase (e.g., Gandhi College) (Satheesh et al., 2017; Zheng et al., 2018).

Compared to GHI, DNI consistently exhibits substantially larger propagated uncertainty ranges across all stations and seasons. Across the analysed stations, seasonal mean DNI uncertainties range from approximately 30 to 49 W m^{-2}, whereas the corresponding GHI uncertainties range between approximately 7 and 18 W m^{-2}. Likewise, the relative seasonal DNI uncertainty (14.6–24.1%) exceeds the corresponding GHI uncertainty (3.0–9.1%) for all station–season combinations considered in this study. This behaviour reflects the stronger sensitivity of the direct solar component to aerosol attenuation and scattering processes (Gueymard, 2012).

The largest propagated DNI uncertainties generally occur during periods of enhanced aerosol loading, particularly over South Asian and North/West African stations. The highest seasonal mean DNI uncertainty (48.8 W m^{-2}) is observed at Zinder Airport during MAM, followed by Karachi during JJA (47.9 W m^{-2}) and Banizoumbou during MAM (47.0 W m^{-2}). More generally, North/West African stations exhibit seasonal mean DNI uncertainties of approximately 40–49 W m^{-2}, associated with periods of enhanced mineral dust activity and, in some regions, biomass-burning aerosols (Di Biagio et al., 2020; Fountoulakis et al., 2021). South Asian stations also exhibit elevated uncertainty levels, with seasonal mean DNI uncertainties typically ranging between 33 and 48 W m^{-2}, while East Asian stations generally display somewhat lower values of approximately 30–42 W m^{-2}. In all cases, increases in aerosol loading are accompanied by considerably larger propagated uncertainties in DNI than in GHI, highlighting the fundamentally different response of direct and global irradiance to aerosol perturbations.

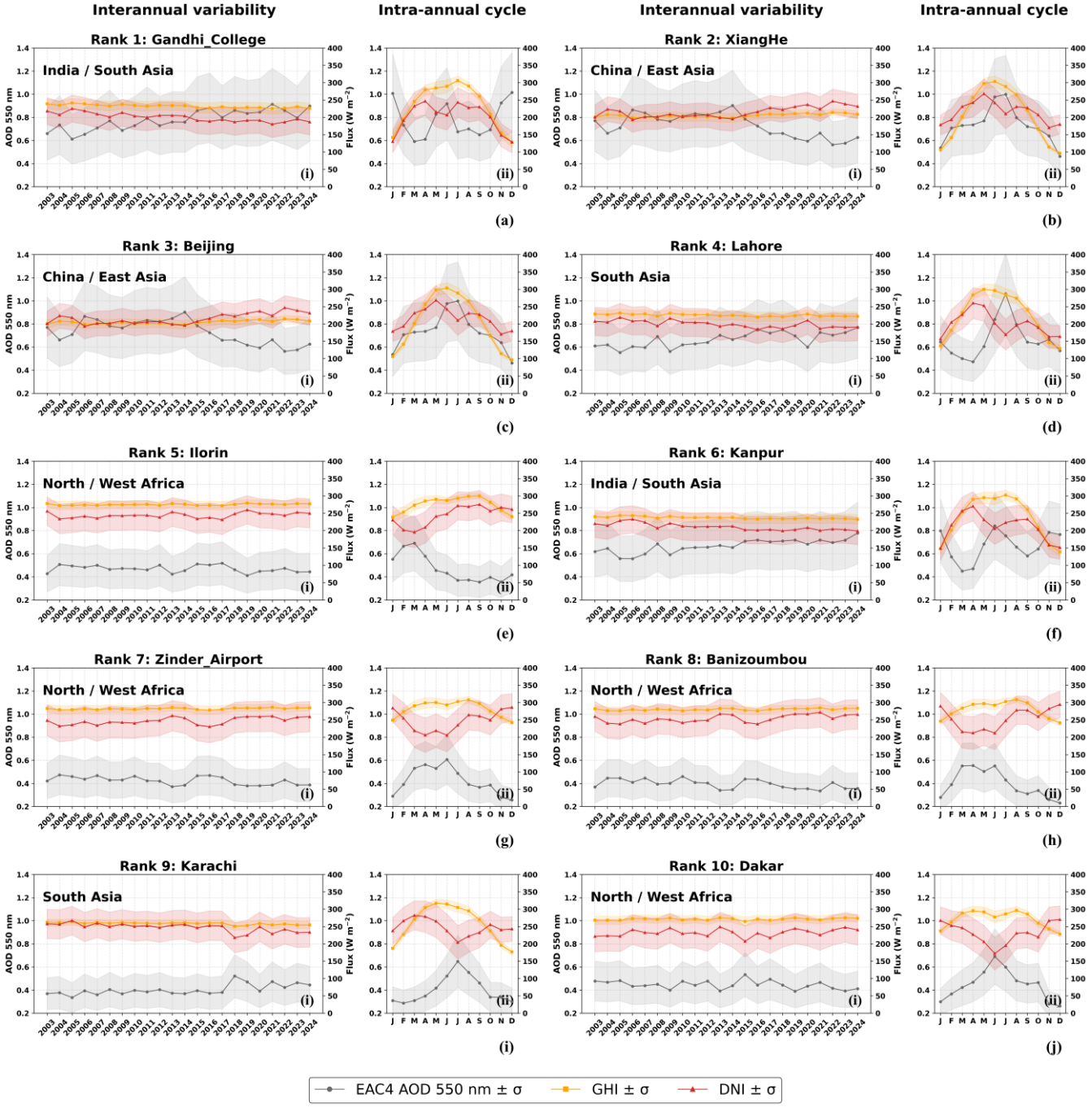

405 **Figure 5: Interannual variability (i) and intra-annual cycle (ii) of aerosol optical depth (AOD) at 550 nm, global horizontal irradiance (GHI), direct normal irradiance (DNI), and their associated propagated uncertainties for the 10 highest-ranked AERONET stations (a)-(j) based on long-term mean AOD. The grey line represents EAC4 AOD at 550 nm, respectively, while the orange and red lines correspond to GHI and DNI. Shaded areas indicate the estimated uncertainty range associated with EAC4 AOD and the propagated uncertainties in GHI and DNI resulting from EAC4 AOD uncertainty. Stations are grouped according to their geographical region,**
410 **with interannual variability shown in the left panels and intra-annual cycles shown in the right panels.**

Despite the elevated aerosol conditions and associated uncertainty ranges, the seasonal behaviour of GHI and DNI remains physically consistent across all stations. Periods characterized by enhanced aerosol loading are generally associated with reductions in DNI due to stronger aerosol extinction of the direct solar beam. The impact on GHI is comparatively weaker because part of the attenuated direct radiation is redistributed into diffuse radiation. Consequently, GHI exhibits smaller uncertainty amplitudes and a more moderate response to aerosol perturbations than DNI, as expected.

Overall, these results highlight the critical importance of accurate aerosol characterization for reliable solar radiation and solar energy assessments. The analysis demonstrates that uncertainties in AOD products can propagate substantially into derived surface irradiance quantities, particularly for DNI under elevated aerosol conditions. Such effects are especially relevant for solar resource applications in regions characterized by persistent pollution or intense dust activity, where aerosol-related uncertainties may significantly influence photovoltaic and concentrating solar power performance assessments (Polo and Estalayo et al., 2015; Neher et al., 2019; Fountoulakis et al., 2021; Hou et al., 2025).

3.4 Evaluation against BSRN

Figure 6 presents the evaluation of the EAC4-derived clear-sky irradiance estimates against the filtered BSRN reference observations, comprising 553,184 clear-sky hourly collocations from 64 BSRN stations distributed globally. Overall, the EAC4-based LUT methodology reproduces clear-sky GHI with excellent accuracy, yielding a correlation coefficient (R) of 1.00, a regression slope of 0.99, a Mean Absolute Error (MAE) of 18.8 W m^{-2}, a standard deviation (STD) of 26.0 W m^{-2}, a Root Mean Square Error (RMSE) of 26.6 W m^{-2}, and a Mean Bias Error (MBE) of −5.9 W m^{-2} (Fig. 6a). The density distribution is tightly concentrated around the one-to-one line, indicating that the EAC4-based approach successfully reproduces both the magnitude and temporal variability of surface GHI over a wide range of atmospheric and geographical conditions. The agreement for clear-sky DNI is lower but remains satisfactory, with R = 0.87, a regression slope of 0.90, a MAE of 62.7 W m^{-2}, a STD of 85.1 W m^{-2}, an RMSE of 89.9 W m^{-2}, and an MBE of −28.9 W m^{-2} (Fig. 6b).

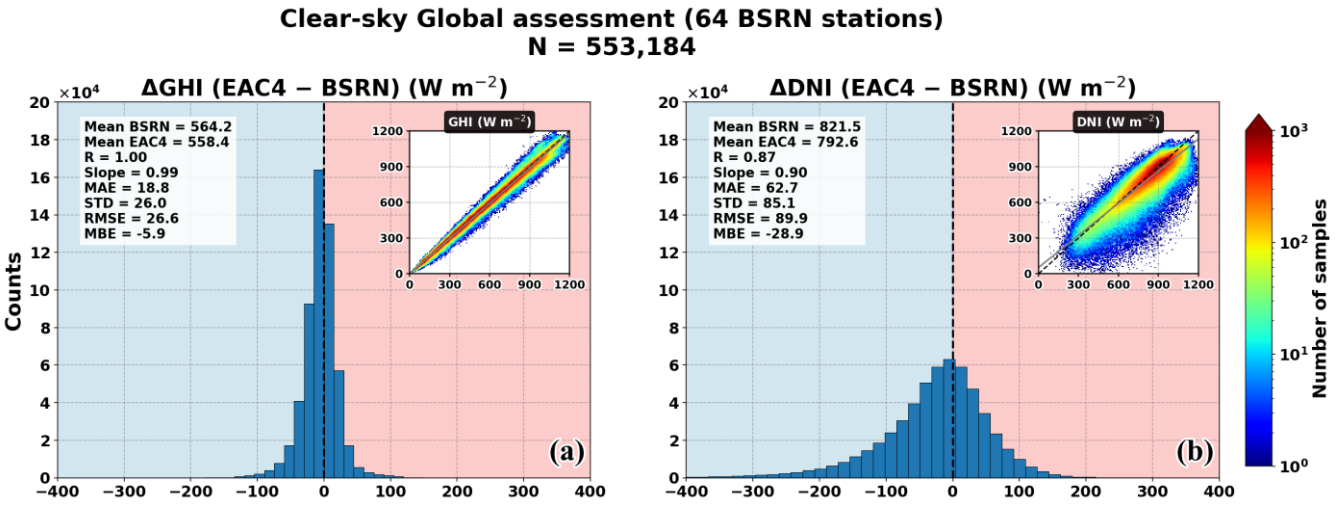

Figure 6: Evaluation of the EAC4-derived clear-sky (a) GHI and (b) DNI estimates against observations from 64 BSRN stations on a global scale for the period 2003–2024. The main panels show the frequency distributions of the irradiance differences (EAC4 − BSRN), with blue and red shading indicating underestimation and overestimation by EAC4, respectively. The statistical metrics reported in each panel include the mean irradiances derived from BSRN and EAC4, the correlation coefficient (R), the regression slope, the mean absolute error (MAE), the standard deviation (STD), the root-mean-square error (RMSE), and the mean bias error (MBE). Insets display density scatter plots of EAC4-derived versus BSRN-observed irradiances, where colours indicate the number of collocated hourly samples in each bin. The black dashed line represents the 1:1 relationship, while the grey solid line denotes the linear regression fit.

To further assess the propagated AOD-related irradiance uncertainties, the absolute differences between the EAC4-derived and BSRN clear-sky irradiances were compared with the corresponding propagated uncertainties for the 553,184 collocations. The mean propagated AOD-related uncertainty was 7.5 W m^{-2} for GHI and 53.1 W m^{-2} for DNI, compared with MAE values of 18.8 and 62.7 W m^{-2}, respectively. These overall statistics are also indicated by the dashed horizontal lines in Fig. S8.

The dependence on aerosol loading was further examined by grouping the collocations into 15 equal-population bins according to EAC4 AOD (Fig. S8). For GHI, the 68th percentile of the absolute EAC4–BSRN difference increased from 18.5 W m^{-2} in the lowest-AOD bin to 27.5 W m^{-2} in the highest-AOD bin, while the corresponding median propagated uncertainty increased from 3.4 to 15.9 W m^{-2}. The response was considerably stronger for DNI, for which the 68th percentile of the observed absolute difference increased from 37.1 to 139.5 W m^{-2}, accompanied by an increase in the median propagated uncertainty from 23.6 to 81.1 W m^{-2}. Thus, increasing aerosol loading is associated with increasing AOD-induced irradiance uncertainty and increasing observed irradiance discrepancies, with a substantially stronger response for DNI.

It should be emphasized that the propagated AOD-related irradiance uncertainty represents only the contribution of EAC4 AOD uncertainty, whereas the EAC4–BSRN differences contain the combined effects of uncertainties in the other atmospheric and surface inputs, radiative-transfer assumptions, spatial representativeness, clear-sky identification, and measurement uncertainty. Consequently, agreement between σ_F and the total observed EAC4–BSRN difference is not expected. The larger difference between these quantities for GHI is also consistent with its lower sensitivity to AOD, whereas the considerably larger propagated DNI uncertainties demonstrate the stronger influence of aerosol uncertainty on direct irradiance.

4 Summary and conclusions

In this study, aerosol optical depth (AOD)-dependent uncertainties for the ECMWF Atmospheric Composition Reanalysis 4 (EAC4) were first derived statistically using collocated EAC4 and Aerosol Robotic NETwork (AERONET) observations following an expected-error (EE) approach. These AOD uncertainties were subsequently propagated into clear-sky solar irradiance estimates over the 2003–2024 period using radiative kernels derived using radiative transfer simulations, enabling the quantification of uncertainties associated with global horizontal irradiance (GHI) and direct normal irradiance (DNI).

The global mean AOD was found to be 0.16, with a corresponding mean estimated AOD uncertainty of 0.07. The resulting global mean relative AOD uncertainty was approximately 47%, although relative uncertainties exceeded 100% over very clean regions because of the EE parameterization and the small absolute AOD values. The uncertainty parameterization represents the statistical distribution of EAC4–AERONET differences over the 2003–2024 period and should therefore be interpreted as an expected statistical uncertainty conditional on EAC4 AOD rather than a dynamically estimated uncertainty for individual atmospheric conditions. The global AOD uncertainties propagated into pronounced spatial and seasonal variability in clear-sky solar irradiance uncertainty. Relative GHI uncertainties generally remained below 5–6% on a global scale, whereas relative DNI uncertainties frequently exceeded 18% over major aerosol source regions and reached annual mean values above 20% locally. Seasonal analyses further showed that regional DNI uncertainties may exceed 25–35% during periods of enhanced aerosol loading, with the largest propagated uncertainties consistently observed over regions affected by persistent anthropogenic pollution, biomass-burning, and desert dust activity.

Station-level analyses performed over the 10 highest-AOD AERONET stations confirmed the strong dependence of propagated irradiance uncertainty on aerosol conditions. Seasonal mean DNI uncertainties ranged between approximately 30 and 49 W m^{-2}, whereas the corresponding GHI uncertainties ranged between 7 and 18 W m^{-2}. The largest uncertainty levels were observed over South Asian and North/West African stations, where persistent anthropogenic pollution and desert dust activity produce elevated aerosol burdens throughout the year. Across these stations, long-term mean AOD values ranged from 0.40 to 0.78, corresponding to mean absolute AOD uncertainties of 0.15–0.27 and relatively consistent relative AOD uncertainties of 34.5–37.0%. These aerosol uncertainties propagated into the solar irradiance estimates, resulting in relative seasonal GHI uncertainties of 3.0–9.1% and relative seasonal DNI uncertainties of 14.6–24.1%. For example, at Gandhi College and Beijing, where long-term mean AOD values reached 0.78 and 0.73, respectively, relative AOD uncertainties remained close to 35%, while the propagated seasonal GHI uncertainties reached approximately 6% and 5.6%, and the corresponding DNI uncertainties approximately 19% and 17%. These findings are consistent with the global uncertainty assessment, which revealed the largest propagated irradiance uncertainties over regions affected by persistent anthropogenic pollution and enhanced desert dust loading.

Finally, the performance of the EAC4-based clear-sky irradiance estimates was evaluated against 553,184 hourly collocations from 64 BSRN stations distributed globally. The results demonstrate excellent agreement for GHI, with R = 1.00, RMSE = 26.6 W m^{-2}, MAE = 18.8 W m^{-2}, and MBE = −5.9 W m^{-2}. For DNI, the agreement remains satisfactory, with R = 0.87, RMSE

= 89.9 W m^{-2}, MAE = 62.7 W m^{-2}, and MBE = −28.9 W m^{-2}, indicating a moderate overall underestimation of direct irradiance. In addition to evaluating the irradiance estimates themselves, the propagated AOD-related uncertainties were assessed against the observed absolute EAC4–BSRN irradiance differences. The observed error distributions increased systematically with the estimated uncertainty, particularly for DNI. When the collocations were stratified by aerosol loading, both the propagated uncertainty and the observed irradiance discrepancies increased with AOD. These results provide an independent assessment that the AOD-based uncertainty framework captures the systematic increase in irradiance discrepancies associated with increasing aerosol loading. However, the propagated uncertainties represent only the contribution from AOD, whereas the observed EAC4–BSRN differences additionally include uncertainties associated with other atmospheric and surface inputs, radiative transfer modelling, representativeness, measurements, and clear-sky classification. Furthermore, the use of monthly climatological SSA and AE does not account for their short-term variability or their potential correlations with aerosol loading and type. Differences between the aerosol optical properties represented by the AeroCom climatology and the aerosol composition in EAC4 may also introduce additional inconsistencies. These limitations can influence both the calculated irradiances and their sensitivity to AOD, particularly for DNI, and should therefore be considered when interpreting the propagated AOD-related uncertainties.

Although cloud variability is the dominant driver of SSR under all-sky conditions, the present analysis focuses on clear-sky irradiance to isolate the contribution of aerosol uncertainty. Such an assessment is particularly relevant for regions combining low cloudiness with elevated aerosol loads, where aerosol effects become a significant source of variability in clear-sky irradiance and where solar energy resources are generally highest. Consequently, accurate characterization of aerosol-induced uncertainty is especially important for solar resource assessment and photovoltaic applications in these regions.

Overall, the results demonstrate that uncertainties in aerosol characterization can propagate substantially into clear-sky irradiance estimates, particularly for DNI. The considerably stronger sensitivity of DNI compared to GHI highlights the importance of accurate aerosol information for solar resource assessment, concentrating solar power applications, and advanced photovoltaic performance studies. The proposed framework provides a computationally efficient approach for generating AOD-related uncertainty estimates for clear-sky solar irradiance at the global scale, while its statistical nature and its focus on AOD alone should be considered when interpreting the resulting uncertainties. It may serve as a basis for future investigations of aerosol-driven dimming and brightening effects, as well as long-term solar energy resource assessments under changing atmospheric conditions. Future developments of this framework will include the generation of MODIS-based irradiance products, enabling a comparison between satellite- and reanalysis-driven irradiance estimates. In addition, the uncertainty propagation analysis will be extended beyond AOD to account for uncertainties in other key aerosol optical properties, particularly the single scattering albedo (SSA), allowing for a more comprehensive characterization of aerosol-induced uncertainties in global irradiances.

Code and data availability

The CAMS global reanalysis (EAC4) data used in this study were obtained from the Copernicus Atmosphere Monitoring Service (CAMS) Atmosphere Data Store (ADS) (Copernicus Atmosphere Monitoring Service, 2020; https://doi.org/10.24381/d58bbf47, accessed on 10 June 2026). The CAMS reanalysis dataset is described in Inness et al. (2019). The Aerosol Robotic Network (AERONET) data are publicly available and can be accessed through the official website at: https://aeronet.gsfc.nasa.gov/. SSR observations from the Baseline Surface Radiation Network (BSRN) (https://bsrn.awi.de/, last access on 17 June 2026) were retrieved through the BSRN FTP archive and processed using the pvlib Python library (Holmgren et al., 2018; Jensen et al., 2023).

Author contributions

Conceptualization, A.M., S.K.; methodology, A.M., S.K., K.P.; software, A.M, K.P., G.C.; validation, A.M., S.K., G.C., K.P.; writing—original draft preparation, A.M; writing—review and editing, A.M., S.K., K.P., G.C.; funding acquisition, S.K. All authors have read and agreed to the published version of the manuscript.

Competing interests

The authors declare that they have no conflict of interest.

Acknowledgements

We gratefully acknowledge the Copernicus Atmosphere Monitoring Service (CAMS) for creating and distributing the CAMS global reanalysis (EAC4) products. We also acknowledge the AERONET network and its principal investigators and site managers for providing high-quality sun-photometer observations, calibration, and data products. Furthermore, we acknowledge the Baseline Surface Radiation Network (BSRN) and the World Radiation Monitoring Center (WMRC) for providing high-quality surface radiation measurements. We sincerely thank the principal investigators, station managers, and technical personnel responsible for the operation, maintenance, and long-term continuity of the AERONET and BSRN stations used in this work. This work was supported by the European Partnership on Metrology through the project 24GRD04 SOLiD-PV. The project (24GRD04 SOLiD-PV) has received funding from the European Partnership on Metrology, co-financed by the European Union's Horizon Europe Research and Innovation Programme and by the Participating States. SK would like to acknowledge Harmonia Action CA21119 supported by COST (European Cooperation in Science and Technology). KP acknowledges the PANORAMA project (Multi-sensor synergies for improved weather-climate-environmental products and applications, to advance European services supporting green transition), funded by the European Union's Horizon Europe Research and Innovation Programme under Grant Agreement No. 101182795. GC would like to acknowledge the

EXCELSIOR project: The EXCELSIOR project has received funding from the European Union's Horizon 2020 Research and Innovation Programme under Grant Agreement No 857510, from the Government of the Republic of Cyprus through the Directorate General for the European Programmes, Coordination and Development and the Cyprus University of Technology.

Financial support This work was financially supported by the European Partnership on Metrology through the project 24GRD04 SOLiD-PV and ACTRIS Switzerland 2025-2028 grant (Swiss contribution to the ACTRIS ERIC) funded by the Swiss State Secretariat for Education and Research and Innovation (SERI).

References

Ahmed, R., Sreeram, V., Mishra, Y., and Arif, M. D.: A review and evaluation of the state-of-the-art in PV solar power forecasting: techniques and optimization, *Renew. Sustain. Energy Rev.*, 124, 109792, https://doi.org/10.1016/j.rser.2020.109792, 2020.

Ångström, A.: On the atmospheric transmission of sun radiation and on dust in the air, *Geogr. Ann.*, 11, 156–166, https://doi.org/10.2307/519399 , 1929.

Arnaoutakis, G., Katsaprakakis, D., and Christakis, D.: Dynamic modeling of combined concentrating solar tower and parabolic trough for increased day-to-day performance, *Appl. Energy*, 323, 119450, https://doi.org/10.1016/j.apenergy.2022.119450 , 2022.

Bartók, B., Wild, M., Folini, D., Lüthi, D., Kotlarski, S., Schär, C., Vautard, R., Jerez, S., and Imecs, Z.: Projected changes in surface solar radiation in CMIP5 global climate models and in EURO-CORDEX regional climate models for Europe, *Clim. Dynam.*, 49, 2665–2683, https://doi.org/10.1007/s00382-016-3471-2 , 2017.

Boucher, O., Randall, D., Artaxo, P., Bretherton, C., Feingold, G., Forster, P., Kerminen, V.-M., Kondo, Y., Liao, H., Lohmann, U., Rasch, P., Satheesh, S. K., Sherwood, S., Stevens, B., and Zhang, X. Y.: Clouds and aerosols, in: *Climate Change 2013: The Physical Science Basis. Contribution of Working Group I to the Fifth Assessment Report of the Intergovernmental Panel on Climate Change*, edited by: Stocker, T. F., Qin, D., Plattner, G.-K., Tignor, M., Allen, S. K., Boschung, J., Nauels, A., Xia, Y., Bex, V., and Midgley, P. M., Cambridge University Press, Cambridge, UK and New York, NY, USA, 571–658, https://doi.org/10.1017/CBO9781107415324.016, 2013.

Buchard, V., Randles, C. A., da Silva, A. M., Darmenov, A., Colarco, P. R., Govindaraju, R., Ferrare, R., Hair, J., Beyersdorf, A. J., Ziemba, L. D., and Yu, H.: The MERRA-2 aerosol reanalysis, 1980 onward. Part II: Evaluation and case studies, *J. Climate*, 30, 6851–6872, https://doi.org/10.1175/JCLI-D-16-0613.1 , 2017.

Chiacchio, M., Ewen, T., Wild, M., Chin, M., and Diehl, T.: Decadal variability of aerosol optical depth in Europe and its relationship to the temporal shift of the North Atlantic Oscillation in the realm of dimming and brightening, *J. Geophys. Res.-Atmos.*, 116, D02109, https://doi.org/10.1029/2010JD014471, 2011.

Diner, D. J., Beckert, J. C., Reilly, T. H., Bruegge, C. J., Conel, J. E., Kahn, R. A., Martonchik, J. V., Ackerman, T. P., Davies, R., Gerstl, S. A. W., Gordon, H. R., Muller, J. P., Myneni, R. B., Sellers, P. J., Pinty, B., and Verstraete, M. M.: Multi-angle imaging spectroradiometer (MISR) instrument description and experiment overview, *IEEE Trans. Geosci. Remote Sens.*, 36, 1072–1087, https://doi.org/10.1109/36.700992, 1998.

Driemel, A., Augustine, J., Behrens, K., Colle, S., Cox, C., Cuevas-Agulló, E., Denn, F. M., Duprat, T., Fukuda, M., Grobe, H., Haeffelin, M., Hodges, G., Hyett, N., Ijima, O., Kallis, A., Knap, W., Kustov, V., Long, C. N., Longenecker, D., Lupi, A., Maturilli, M., Mimouni, M., Ntsangwane, L., Ogihara, H., Olano, X., Olefs, M., Omori, M., Passamani, L., Pereira, E. B., Schmithüsen, H., Schumacher, S., Sieger, R., Tamlyn, J., Vogt, R., Vuilleumier, L., Xia, X., Ohmura, A., and König-Langlo, G.: Baseline Surface Radiation Network (BSRN): structure and data description (1992–2017), Earth Syst. Sci. Data, 10, 1491–1501, https://doi.org/10.5194/essd-10-1491-2018 , 2018.

Di Biagio, C., Balkanski, Y., Albani, S., Boucher, O., and Formenti, P.: Direct radiative effect by mineral dust aerosols constrained by new microphysical and spectral optical data, *Geophys. Res. Lett.*, 47, e2019GL086186, https://doi.org/10.1029/2019GL086186, 2020.

Eck, T. F., Holben, B. N., Reid, J. S., Dubovik, O., Smirnov, A., O'Neill, N. T., Slutsker, I., and Kinne, S.: Wavelength dependence of the optical depth of biomass burning, urban, and desert dust aerosols, *J. Geophys. Res.-Atmos.*, 104, 31333–31349, https://doi.org/10.1029/1999JD900923 , 1999.

Flemming, J., Huijnen, V., Arteta, J., Bechtold, P., Beljaars, A., Blechschmidt, A.-M., Diamantakis, M., Engelen, R. J., Gaudel, A., Inness, A., Jones, L., Josse, B., Katragkou, E., Marécal, V., Peuch, V.-H., Richter, A., Schultz, M. G., Stein, O., and Tsikerdekis, A.: Tropospheric chemistry in the Integrated Forecasting System of ECMWF, Geosci. Model Dev., 8, 975–1003, https://doi.org/10.5194/gmd-8-975-2015 , 2015.

Fountoulakis, I., Kosmopoulos, P., Papachristopoulou, K., Raptis, I. P., Mamouri, R. E., Nisantzi, A., Gkikas, A., Witthuhn, J., Bley, S., Moustaka, A., Buehl, J., Seifert, P., Hadjimitsis, D. G., Kontoes, C., and Kazadzis, S.: Effects of aerosols and clouds on the levels of surface solar radiation and solar energy in Cyprus, *Remote Sens.-Basel*, 13, 2319, https://doi.org/10.3390/rs13122319, 2021.

Gelaro, R., McCarty, W., Suárez, M. J., Todling, R., Molod, A., Takacs, L., Randles, C. A., Darmenov, A., Bosilovich, M. G., Reichle, R., Wargan, K., Coy, L., Cullather, R., Draper, C., Akella, S., Buchard, V., Conaty, A., da Silva, A. M., Gu, W., Kim, G.-K., Koster, R., Lucchesi, R., Merkova, D., Nielsen, J. E., Partyka, G., Pawson, S., Putman, W., Rienecker, M., Schubert, S. D., Sienkiewicz, M., and Zhao, B.: The Modern-Era Retrospective Analysis for Research and Applications, Version 2 (MERRA-2), *J. Climate*, 30, 5419–5454, https://doi.org/10.1175/JCLI-D-16-0758.1, 2017.

Giles, D. M., Sinyuk, A., Sorokin, M. G., Schafer, J. S., Smirnov, A., Slutsker, I., Eck, T. F., Holben, B. N., Lewis, J. R., Campbell, J. R., Welton, E. J., Korkin, S. V., and Lyapustin, A. I.: Advancements in the Aerosol Robotic Network (AERONET) Version 3 database – automated near-real-time quality control algorithm with improved cloud screening for Sun photometer aerosol optical depth (AOD) measurements, *Atmos. Meas. Tech.*, 12, 169–209, https://doi.org/10.5194/amt-12-169-2019, 2019.

Gkikas, A., Houssos, E. E., Lolis, C. J., Bartzokas, A., Mihalopoulos, N., and Hatzianastassiou, N.: Atmospheric circulation evolution related to desert-dust episodes over the Mediterranean, *Q. J. Roy. Meteor. Soc.*, 141, 1634–1645, https://doi.org/10.1002/qj.2466 , 2015.

Gueymard, C.: Critical analysis and performance assessment of clear-sky solar irradiance models using theoretical and measured data, *Sol. Energy*, 51, 121–138, https://doi.org/10.1016/0038-092X(93)90074-X, 1993.

Gueymard, C.: Variability in direct irradiance around the Sahara: Are the modeled datasets of bankable quality?, in: *SolarPACES Conference 2010*, Perpignan, France, available at: https://www.academia.edu/29425719/Variability_in_direct_irradiance_around_the_Sahara_Are_the_modeled_datasets_of_bankable_quality (last access: 8 July 2025), 2010.

Gueymard, C. A.: Temporal variability in direct and global irradiance at various time scales as affected by aerosols, *Sol. Energy*, 86, 3544–3553, https://doi.org/10.1016/j.solener.2012.01.013, 2012.

Granier, C., Bessagnet, B., Bond, T., D'Angiola, A., Denier van der Gon, H., Frost, G. J., Heil, A., Kaiser, J. W., Kinne, S., Klimont, Z., Kloster, S., Lamarque, J.-F., Liousse, C., Masui, T., Meleux, F., Mieville, A., Ohara, T., Raut, J.-C., Riahi, K., Schultz, M. G., Smith, S. J., Thompson, A., van Aardenne, J., van der Werf, G. R., and van Vuuren, D. P.: Evolution of anthropogenic and biomass burning emissions of air pollutants at global and regional scales during the 1980–2010 period, Climatic Change, 109, 163–190, https://doi.org/10.1007/s10584-011-0154-1 , 2011.

Gui, K., Che, H., Zheng, Y., Wang, Y., Zhang, L., Zhao, H., Li, L., Zhong, J., Yao, W., and Zhang, X.: Seasonal variability and trends in global type-segregated aerosol optical depth as revealed by MISR satellite observations, *Sci. Total Environ.*, 787, 147543, https://doi.org/10.1016/j.scitotenv.2021.147543, 2021.

Emde, C., Buras-Schnell, R., Kylling, A., Mayer, B., Gasteiger, J., Hamann, U., Kylling, J., Richter, B., Pause, C., Dowling, T., and Bugliaro, L.: The libRadtran software package for radiative transfer calculations (version 2.0.1), Geosci. Model Dev., 9, 1647–1672, https://doi.org/10.5194/gmd-9-1647-2016 , 2016.

Hatzianastassiou, N., Ioannidis, E., Korras-Carraca, M.-B., Gavrouzou, M., Papadimas, C. D., Matsoukas, C., Benas, N., Fotiadi, A., Wild, M., and Vardavas, I.: Global dimming and brightening features during the first decade of the 21st century, *Atmosphere*, 11, 308, https://doi.org/10.3390/atmos11030308, 2020.

He, J., Hong, L., Shao, C., and Tang, W.: Global evaluation of simulated surface shortwave radiation in CMIP6 models, *Atmos. Res.*, 292, 106896, https://doi.org/10.1016/j.atmosres.2023.106896, 2023.

Holben, B. N., Tanré, D., Smirnov, A., Eck, T. F., Slutsker, I., Abuhassan, N., Newcomb, W. W., Schafer, J. S., Chatenet, B., Lavenu, F., Kaufman, Y. J., Vande Castle, J., Setzer, A., Markham, B., Clark, D., Frouin, R., Halthore, R., Karneli, A., O'Neill, N. T., Pietras, C., Pinker, R. T., Voss, K., and Zibordi, G.: An emerging ground-based aerosol climatology: Aerosol optical depth from AERONET, *J. Geophys. Res.-Atmos.*, 106, 12067–12097, https://doi.org/10.1029/2001JD900014, 2001.

Holben, B. N., Eck, T. F., Slutsker, I., Tanré, D., Buis, J. P., Setzer, A., Vermote, E., Reagan, J. A., Kaufman, Y. J., Nakajima, T., Lavenu, F., Jankowiak, I., and Smirnov, A.: AERONET—A federated instrument network and data archive for aerosol characterization, *Remote Sens. Environ.*, 66, 1–16, https://doi.org/10.1016/S0034-4257(98)00031-5, 1998.

Holmgren, W. F., W. Hansen, C., and A. Mikofski, M.: pvlib python: a python package for modeling solar energy systems. *Journal of Open Source Software*, *3*(29), 884. https://doi.org/10.21105/joss.00884, 2018.

Hou, X., Papachristopoulou, K., and Kazadzis, S.: Assessment of aerosol optical depth forecast for day-ahead clear-sky direct irradiance, *Atmos. Meas. Tech.*, 18, 4543–4557, https://doi.org/10.5194/amt-18-4543-2025, 2025.

Hu, Y., Prasad, A., and Kay, M.: Smart integration of aerosols for DNI predictions in Australia using LSTM, *Sol. Energy*, 316, 114855, https://doi.org/10.1016/j.solener.2026.114855, 2026.

Huijnen, V., Williams, J., van Weele, M., van Noije, T., Krol, M., Dentener, F., Segers, A., Houweling, S., Peters, W., de Laat, J., Boersma, F., Bergamaschi, P., van Velthoven, P., Le Sager, P., Eskes, H., Alkemade, F., Scheele, R., Nédélec, P., and Pätz, H.-W.: The global chemistry transport model TM5: description and evaluation of the tropospheric chemistry version 3.0, *Geosci. Model Dev.*, 3, 445–473, https://doi.org/10.5194/gmd-3-445-2010, 2010.

IEA: Renewables 2025– Analysis and forecast to 2026, https://www.iea.org/reports/renewables-2025 (last access: 11 June 2026), 2025.

Inness, A., Ades, M., Agustí-Panareda, A., Barré, J., Benedictow, A., Blechschmidt, A.-M., Dominguez, J. J., Engelen, R., Eskes, H., Flemming, J., Huijnen, V., Jones, L., Kipling, Z., Massart, S., Parrington, M., Peuch, V.-H., Razinger, M., Rémy, S., Schulz, M., and Suttie, M.: The CAMS reanalysis of atmospheric composition, *Atmos. Chem. Phys.*, 19, 3515–3556, https://doi.org/10.5194/acp-19-3515-2019, 2019.

Izam, N. S. M. N., Itam, Z., Sing, W. L., and Syamsir, A.: Sustainable development perspectives of solar energy technologies with focus on solar photovoltaic—A review, *Energies*, 15, 2790, https://doi.org/10.3390/en15082790, 2022.

Jensen, A. R., Anderson, K. S., Holmgren, W. F., Mikofski, M. A., Hansen, C. W., Boeman, L. J., and Loonen, R.: pvlib iotools—Open-source Python functions for seamless access to solar irradiance data. *Solar Energy*, 266, 112092. https://doi.org/10.1016/j.solener.2023.112092, 2023.

Jiao, B., Li, Q., Sun, W., and Wild, M.: Uncertainties in the global and continental surface solar radiation variations: Inter-comparison of in-situ observations, reanalyses, and model simulations, *Clim. Dynam.*, 59, 2499–2516, https://doi.org/10.1007/s00382-022-06222-3, 2022.

Kaiser, J. W., Heil, A., Andreae, M. O., Benedetti, A., Chubarova, N., Jones, L., Morcrette, J.-J., Razinger, M., Schultz, M. G., Suttie, M., and van der Werf, G. R.: Biomass burning emissions estimated with a global fire assimilation system based on observed fire radiative power, Biogeosciences, 9, 527–554, https://doi.org/10.5194/bg-9-527-2012, 2012.

Kazadzis, S., Kouremeti, N., Nyeki, S., Gröbner, J., and Wehrli, C.: The World Optical Depth Research and Calibration Center (WORCC) quality assurance and quality control of GAW-PFR AOD measurements, Geosci. Instrum. Method. Data Syst., 7, 39– 53, https://doi.org/10.5194/gi-7-39-2018 , 2018.

Kinne, S.: The MACv2 aerosol climatology, *Tellus B*, 71, 1623639, https://doi.org/10.1080/16000889.2019.1623639, 2019.

Levy, R. C., Remer, L. A., Kleidman, R. G., Mattoo, S., Ichoku, C., Kahn, R., and Eck, T. F.: Global evaluation of the Collection 5 MODIS dark-target aerosol products over land, Atmos. Chem. Phys., 10, 10399–10420, https://doi.org/10.5194/acp-10-10399-2010, 2010.

Kok, J. F., Storelvmo, T., Karydis, V. A., Adebiyi, A. A., Mahowald, N. M., Evan, A. T., He, C., and Leung, D. M.: Mineral dust aerosol impacts on global climate and climate change, *Nat. Rev. Earth Environ.*, 4, 71–86, https://doi.org/10.1038/s43017-022-00379-5 , 2023.

Langerock, B., Arola, A., Benedictow, A., Bennouna, Y., Blake, L., Bouarar, I., Cuevas, E., Errera, Q., Eskes, H. J., Griesfeller, J., Ilić, L., Kapsomenakis, J., Li, C. W. Y., Mortier, A., Pison, I., Pitkänen, M., Richter, A., Schoenhardt, A., Schulz, M., Tarniewicz, J., Tsikerdekis, A., Warneke, T., and Zerefos, C.: Validation report for the CAMS global reanalyses of aerosol and reactive trace gases: 2003–2023, Copernicus Atmosphere Monitoring Service (CAMS) Report, CAMS2_82_2023SC2_D82.4.2.1-2024, https://doi.org/10.24380/g8h7-kd21 , 2024.

Li, Z., Yang, J., and Dezfuli, P. A. N.: Study on the influence of light intensity on the performance of solar cell, *Int. J. Photoenergy*, 2021, 6648739, https://doi.org/10.1155/2021/6648739, 2021.

Long, C. N., and Ackerman, T. P.: Identification of clear skies from broadband pyranometer measurements and calculation of downwelling shortwave cloud effects, J. Geophys. Res. Atmos., 105(D12), 15609–15626, https://doi.org/10.1029/2000JD900077, 2000.

Lu, Y.-B., Wang, L.-C., Zhou, J.-J., Niu, Z.-G., Zhang, M., and Qin, W.-M.: Assessment of the high-resolution estimations of global and diffuse solar radiation using WRF-Solar, *Adv. Clim. Change Res.*, 14, 720–731, https://doi.org/10.1016/j.accre.2023.09.009, 2023.

McComiskey, A., Schwartz, S. E., Schmid, B., Guan, H., Lewis, E. R., Ricchiazzi, P., and Ogren, J. A.: Direct aerosol forcing: Calculation from observables and sensitivities to inputs, *J. Geophys. Res.-Atmos.*, 113, D09202, https://doi.org/10.1029/2007JD009170, 2008.

Moustaka, A., Gkikas, A., Logothetis, S.-A., Flemming, J., Rémy, S., Ades, M., Benedetti, A., Tourpali, K., Amiridis, V., and Kazadzis, S.: Two decades of aerosol optical depth evolution from CAMS reanalysis, *EGUsphere* [preprint], https://doi.org/10.5194/egusphere-2026-1107, 2026.

Morcrette, J.-J., Boucher, O., Jones, L., Salmond, D., Bechtold, P., Beljaars, A., Benedetti, A., Bonet, A., Kaiser, J. W., Razinger, M., Schulz, M., Serrar, S., Simmons, A. J., Sofiev, M., Suttie, M., Tompkins, A. M., and Untch, A.: Aerosol analysis and forecast in the European Centre for Medium-Range Weather Forecasts Integrated Forecast System: Forward modeling, *J. Geophys. Res.*, 114, D06206, https://doi.org/10.1029/2008JD011235, 2009.

Mueller, R. W., Matsoukas, C., Gratzki, A., Behr, H. D., and Hollmann, R.: The CM-SAF operational scheme for the satellite based retrieval of solar surface irradiance – a LUT-based eigenvector hybrid approach, *Remote Sens. Environ.*, 113, 1012–1024, https://doi.org/10.1016/j.rse.2009.01.012, 2009.

Neher, I., Eck, M., Schürmann, G. J., Hirsch, T., and Kandler, K.: Impact of atmospheric aerosols on solar power, *Meteorol. Z.*, 28, 239–249, https://doi.org/10.1127/metz/2019/0969, 2019.

Ohmura, A., Gilgen, H., Hegner, H., Müller, G., Wild, M., Dutton, E. G., Forgan, B., Fröhlich, C., Philipona, R., Heimo, A., König-Langlo, G., McArthur, B., Pinker, R., Whitlock, C. H., and Dehne, K.: Baseline Surface Radiation Network

(BSRN/WCRP): New Precision Radiometry for Climate Research. *Bulletin of the American Meteorological Society*, *79*(10), 2115–2136. https://doi.org/10.1175/1520-0477(1998)079<2115:BSRNBW>2.0.CO;2, 1998.

Papachristopoulou, K., Fountoulakis, I., Bais, A. F., Psiloglou, B. E., Papadimitriou, N., Raptis, I.-P., Kazantzidis, A., Kontoes, C., Hatzaki, M., and Kazadzis, S.: Effects of clouds and aerosols on downwelling surface solar irradiance nowcasting and short-term forecasting, *Atmos. Meas. Tech.*, 17, 1851–1877, https://doi.org/10.5194/amt-17-1851-2024, 2024.

Papachristopoulou, K., Fountoulakis, I., Gkikas, A., Kosmopoulos, P. G., Nastos, P. T., Hatzaki, M., and Kazadzis, S.: 15-year analysis of direct effects of total and dust aerosols in solar radiation/energy over the Mediterranean Basin, *Remote Sens.-Basel*, 14, 1535, https://doi.org/10.3390/rs14071535, 2022.

Polo, J. and Estalayo, G.: Impact of atmospheric aerosol loads on concentrating solar power production in arid-desert sites, *Sol. Energy*, 115, 621–631, https://doi.org/10.1016/j.solener.2015.03.031, 2015.

Roccetti, G., Bugliaro, L., Gödde, F., Emde, C., Hamann, U., Manev, M., Sterzik, M. F., and Wehrum, C.: HAMSTER: Hyperspectral albedo maps dataset with high spatial and temporal resolution, *Atmos. Meas. Tech.*, 17, 6025–6046, https://doi.org/10.5194/amt-17-6025-2024, 2024.

Satheesh, S. K., Babu, S. S., Padmakumari, B., Pandithurai, G., and Soni, V. K.: Variability of atmospheric aerosols over India, in: *Observed Climate Variability and Change over the Indian Region*, edited by: Krishnan, R., Sanjay, J., Gnanaseelan, C., Mujumdar, M., Kulkarni, A., and Chakraborty, S., Springer, Singapore, 221–248, https://doi.org/10.1007/978-981-10-2531-0_13, 2017.

Saint-Drenan, Y. M., and Wald, L.: On the assessment of hourly means of solar irradiance at ground level in clear-sky conditions by the ERA5, JRA-3Q, and MERRA-2 reanalyses, Atmosphere, 16, 949, https://doi.org/10.3390/atmos16080949, 2025.

Sayer, A. M., Hsu, N. C., Bettenhausen, C., and Jeong, M. J.: Validation and uncertainty estimates for MODIS Collection 6 "Deep Blue" aerosol data, *J. Geophys. Res.-Atmos.*, 118, 7864–7872, https://doi.org/10.1002/jgrd.50600, 2013.

Şen, Z.: Solar energy in progress and future research trends, *Prog. Energy Combust. Sci.*, **30**, 367–416, https://doi.org/10.1016/j.pecs.2004.02.004 , 2004.

Sengupta, M., Habte, A., Wilbert, S., Gueymard, C., and Remund, J.: Best Practices Handbook for the Collection and Use of Solar Resource Data for Solar Energy Applications: Third Edition, Tech. Rep. NREL/TP-5D00-77635, 1778700, MainId:29561, NREL, https://doi.org/10.2172/1778700 , 2021

Shell, K. M., Kiehl, J. T., and Shields, C. A.: Using the radiative kernel technique to calculate climate feedbacks in NCAR's Community Atmospheric Model, *J. Climate*, 21, 2269–2282, https://doi.org/10.1175/2007JCLI2044.1, 2008.

Sinyuk, A., Holben, B. N., Eck, T. F., Giles, D. M., Slutsker, I., Korkin, S., Schafer, J. S., Smirnov, A., Sorokin, M., and Lyapustin, A.: The AERONET Version 3 aerosol retrieval algorithm, associated uncertainties and comparisons to Version 2, *Atmos. Meas. Tech.*, 13, 3375–3411, https://doi.org/10.5194/amt-13-3375-2020, 2020.

Soden, B. J., Held, I. M., Colman, R., Shell, K. M., Kiehl, J. T., and Shields, C. A.: Quantifying climate feedbacks using radiative kernels, *J. Climate*, 21, 3504–3520, https://doi.org/10.1175/2007JCLI2110.1 , 2008.

Stuut, J.-B., Boersen, B., Brück, H. M., Hansen, A., Koster, B., van der Does, M., and Witte, Y.: TRAFFIC: Transatlantic Fluxes of Saharan Dust – Cruise No. M89, 3–25 October 2012, Las Palmas de Gran Canaria (Spain) – Cristobal (Panama), METEOR-Berichte, M89, DFG-Senatskommission für Ozeanographie, Bremen, Germany, 30 pp., https://doi.org/10.2312/cr_m89, 2014.

Qu, Z., Oumbe, A., Blanc, P., Espinar, B., Gesell, G., Gschwind, B., Klüser, L., Lefèvre, M., Saboret, L., Schroedter-Homscheidt, M., and Wald, L.: Fast radiative transfer parameterisation for assessing the surface solar irradiance: The Heliosat-4 method, *Meteorol. Z.*, 26, 33–57, https://doi.org/10.1127/metz/2016/0781, 2017.

Tang, W., Yang, K., Qin, J., Min, M., Liang, S., and Lu, N.: A 16-year dataset (2000–2015) of high-resolution (3 h, 10 km) global surface solar radiation, *Earth Syst. Sci. Data*, 11, 1905–1915, https://doi.org/10.5194/essd-11-1905-2019, 2019.

Thorsen, T. J., Winker, D. M., and Ferrare, R. A.: Uncertainty in observational estimates of the aerosol direct radiative effect and forcing, *J. Climate*, 34, 195–214, https://doi.org/10.1175/JCLI-D-19-1009.1, 2021.

Thorsen, T. J., Ferrare, R. A., Kato, S., and Winker, D. M.: Aerosol direct radiative effect sensitivity analysis, *J. Climate*, 33, 6119–6139, https://doi.org/10.1175/JCLI-D-19-0669.1, 2020.

SolarPowerEurope: Global Market Outlook For Solar Power 2025-2030, https://www.solarpowereurope.org/insights/outlooks/eu-solar-market-outlook-2025-2030 (last access: 11 June 2026), 2025.

Wang, Y., Zhang, D., Ji, Q., and Shi, X.: Regional renewable energy development in China: A multidimensional assessment, *Renew. Sustain. Energy Rev.*, 124, 109797, https://doi.org/10.1016/j.rser.2020.109797 , 2020.

Wild, M., Folini, D., Schär, C., Loeb, N., Dutton, E. G., and König-Langlo, G.: The global energy balance from a surface perspective, *Clim. Dynam.*, 40, 3107–3134, https://doi.org/10.1007/s00382-012-1569-8 , 2013.

Wiltink, J. I., Deneke, H., Saint-Drenan, Y.-M., van Heerwaarden, C. C., and Meirink, J. F.: Validating global horizontal irradiance retrievals from Meteosat SEVIRI at increased spatial resolution against a dense network of ground-based observations, Atmos. Meas. Tech., 17, 6003–6024, https://doi.org/10.5194/amt-17-6003-2024 , 2024.

Witthuhn, J., Hünerbein, A., Filipitsch, F., Wacker, S., Meilinger, S., and Deneke, H.: Aerosol properties and aerosol–radiation interactions in clear-sky conditions over Germany, *Atmos. Chem. Phys.*, 21, 14591–14630, https://doi.org/10.5194/acp-21-14591-2021, 2021.

Xu, X., Vignarooban, K., Xu, B., Hsu, K., and Kannan, A. M.: Prospects and problems of concentrating solar power technologies for power generation in the desert regions, *Renew. Sustain. Energy Rev.*, 53, 1106–1131, https://doi.org/10.1016/j.rser.2015.09.015, 2016.

Yang, D., Wang, W., Gueymard, C. A., Hong, T., Kleissl, J., Huang, J., Perez, M. J., Perez, R., Bright, J. M., Xia, X., van der Meer, D., and Peters, I. M.: A review of solar forecasting, its dependence on atmospheric sciences and implications for grid integration: Towards carbon neutrality, *Renew. Sustain. Energy Rev.*, 161, 112348, https://doi.org/10.1016/j.rser.2022.112348, 2022.

Zhang, Z., Li, J., Che, H., Dong, Y., Dubovik, O., Eck, T., Gupta, P., Holben, B., Kim, J., Lind, E., Saud, T., Tripathi, S. N., and Ying, T.: Long-term trends in aerosol properties derived from AERONET measurements, *Atmos. Chem. Phys.*, 25, 4617–4637, https://doi.org/10.5194/acp-25-4617-2025 , 2025.

Zheng, B., Tong, D., Li, M., Liu, F., Hong, C., Geng, G., Li, H., Li, X., Peng, L., Qi, J., Yan, L., Zhang, Y., Zhao, H., Zheng, Y., He, K., and Zhang, Q.: Trends in China's anthropogenic emissions since 2010 as the consequence of clean air actions, *Atmos. Chem. Phys.*, 18, 14095–14111, https://doi.org/10.5194/acp-18-14095-2018, 2018.

Zib, B. J., Dong, X., Xi, B., and Kennedy, A.: Evaluation and intercomparison of cloud fraction and radiative fluxes in recent reanalyses over the Arctic using BSRN surface observations, *J. Climate*, 25, 2291–2305, https://doi.org/10.1175/JCLI-D-11-00147.1, 2012.